Check for updates

Advanced Functional Materials

ADVANCED FUNCTIONAL MATERIALS
www.afm-journal.de

RESEARCH ARTICLE OPEN ACCESS

Exploring Pb-Chelation Chemistry in the Crystallization Dynamics of Halide Perovskites

Byeong Jun Kim[1] | Inseo Cho[2] | Jung Geon Son[3,4] | Yifan Yu[1] | Gunhee Kim[1] | Eunseo Shin[1] | Seyeon Eom[1] | Minsub Um[2] | Subeom Shin[2] | Hyungju Ahn[5] | Dong Suk Kim[3,4,6] | Hochan Song[2,7] | Hyosung Choi[1] | Jonghee Yang[2]

[1]Department of Chemistry, Hanyang University, Seoul, Republic of Korea | [2]Department of Chemistry, Yonsei University, Seoul, Republic of Korea | [3]Graduate School of Carbon Neutrality, Ulsan National Institute of Science and Technology (UNIST), Ulsan, Republic of Korea | [4]UNIST InnoCORE AI-Space Solar Initiative, Ulsan National Institute of Science and Technology (UNIST), Ulsan, Republic of Korea | [5]Pohang Accelerator Laboratory, POSTECH, Pohang, Republic of Korea | [6]School of Energy and Chemical Engineering, Ulsan National Institute of Science and Technology (UNIST), Ulsan, Republic of Korea | [7]Institute For Advanced Materials and Manufacturing, Department of Materials Science and Engineering, The University of Tennessee, Knoxville, Tennessee, USA

Correspondence: Dong Suk Kim (kimds@unist.ac.kr) | Hochan Song (hsong19@utk.edu) | Hyosung Choi (hschoi202@hanyang.ac.kr) | Jonghee Yang (jhyang@yonsei.ac.kr)

Received: 3 February 2026 | **Revised:** 1 April 2026 | **Accepted:** 4 May 2026

ABSTRACT

Crystallization of halide perovskites (HP) is strongly entangled with a meticulous equilibrium in precursor states. Molecular coordination with metal ions, via chelating additives, has emerged as an effective strategy to regulate this process, yet the details of their associated chemistry are rarely explored. Here, we explore the chelation behavior of the representative ethylenediaminetetraacetic acid (EDTA) toward Pb^{2+} in HP precursors and show that the deprotonation state crucially alters the coordination scenario and the subsequent crystallization pathways of HP matrices. We found that the fully deprotonated $EDTA^{4-}$ achieves a more rigorous chelation with Pb^{2+} than the $EDTA^{2-}$ counterpart, suppressing the iodoplumbate aggregates in solution responsible for local PbI_2 heterogeneity in the films. Furthermore, $EDTA^{4-}$ incorporation promotes the nucleation of defect-free and aligned HP lattices that manifest coherent lattice growth during crystallization, attributed to the chemical reconstruction of the cluttered lattice sites that eliminate surface HP defects. As a result, the $EDTA^{4-}$ incorporated HP matrices exhibit improved structural and energetic homogeneity, resulting in improved solar cell performance. Our findings provide mechanistic insight into crystallization control and highlight that tuning precursor coordination through the deprotonation state of chelating additive enables molecular-scale regulation of precursor chemistry to drive macroscopic improvements in device performance.

1 | Introduction

Halide perovskite (HP)-based solar cells (PSCs) have emerged as the frontrunners of next-generation photovoltaics, combining exceptional optoelectronic properties and rapidly improving power conversion efficiency (PCE) [1–3], while their low-temperature, solution-processable fabrication offers a promising route toward scalable and low-cost photovoltaics [4–7]. Despite these advances, reproducible demonstration of PSCs with high PCEs remains challenging, as HP film formation during solution processing is highly sensitive to crystallization pathways. Due to the non-equilibrium fabrication processes involving abrupt chemical changes in the reaction system, the consequent rapid nucleation and crystal growth can induce structural

Byeong Jun Kim, Inseo Cho, and Jung Geon Son contributed equally to this work.

This is an open access article under the terms of the Creative Commons Attribution License, which permits use, distribution and reproduction in any medium, provided the original work is properly cited.
© 2026 The Author(s). *Advanced Functional Materials* published by Wiley-VCH GmbH

inhomogeneity such as undesired phases or random crystal orientations, and a high density of defects in polycrystalline HP films [8–10]. These structural imperfections lead to an inhomogeneous energy landscape, hindering carrier transport and promoting carrier trapping at defective regions (e.g., grain boundaries and phase-impure domains), thereby enhancing non-radiative recombination and causing efficiency losses [11–13]. Moreover, the degradation processes of HP phases are accelerated at such defect regions, thereby compromising long-term device stability [14, 15]. Thus, achieving robust device reliability requires precise control over crystallization kinetics and phase evolution to ensure superior structural integrity [11, 16, 17].

From a fundamental viewpoint, the crystallization pathway is governed by precursor-solution chemistry, where solute–solvent interactions and the coordination environment of Pb^{2+} determine nucleation and subsequent crystal growth [13, 18–20]. In I-rich precursor solutions used for HP deposition, in general, PbI_2 does not fully dissociate into isolated Pb^{2+} and I^- ions. Instead, PbI_2 readily coordinates with excess I^- to form iodoplumbate complexes (i.e., $[PbI_x]^{2-x}$) that are in dynamic chemical equilibrium, which tend to form cluster-like aggregates acting as prenucleation species [13, 21, 22]. While the large-sized colloidal aggregates, as a result of such delicate equilibria, can serve as nuclei to be transformed into a large-grain HP domain in the polycrystalline matrices, this spatially impedes the full engagement of A-site cations rendering non-HP local crystallites (e.g., PbI_2 and hexagonal δ-phases) [10, 23–25]. These findings suggest that the control over the chemical state of iodoplumbate complex in the precursor solution is a key prerequisite for achieving homogeneous and coherent crystalline films and mitigating defect formation [10, 13, 21–24, 26].

Extensive efforts have focused on modulating Pb—I coordination through solvent and additive engineering to control iodoplumbate complexes in the precursor solution [18, 27]. Lewis-base solvents with high donor numbers have been widely employed to coordinate Pb^{2+} and weaken Pb—I interactions, thereby improving precursor homogeneity [20, 28]. Furthermore, additives with functional groups based on elements with lone pairs, such as N, O, and S, have been employed to form coordination bonds with Pb^{2+}, with the aim of controlling the size and distribution of iodoplumbate clusters and thereby controlling crystallization kinetics. Among these, chelating additives capable of multidentate binding can form stronger and more stable Pb^{2+}–ligand complexes and are therefore attracting attention [29–32]. Since such chelating additives typically contain multiple functional groups, they can exist in several protonation/deprotonation states in solution, each associated with distinct charge states and coordination modes. Previous studies indicate that increasing deprotonation enhances the availability of anionic donor sites (e.g., carboxylates), thereby strengthening the chelation/coordination capability toward Pb^{2+} [33, 34]. This suggests that the degree of deprotonation of the chelating additive should be treated as a key design parameter for precisely tuning Pb^{2+}–I coordination equilibria and the speciation of iodoplumbate complexes in HP precursor solutions.

In this study, we demonstrate that the deprotonation state of a chelating additive decisively governs coordination chemistry and HP crystallization behavior. Using ethylenediaminetetraacetic acid (EDTA) salts as a model system, we examine how distinct chelation environments around Pb^{2+} regulate iodoplumbate clustering in precursor solutions by comparing partially and fully deprotonated EDTA ($EDTA^{2-}$ and $EDTA^{4-}$). We find that the EDTA deprotonation state defines the chemical nature of the chelation environment; $EDTA^{4-}$, with four uniformly deprotonated carboxylates, exhibits a more distinct and rigorous chelation with Pb^{2+} and interaction with FA^+, thereby more effectively suppressing iodoplumbate aggregates that otherwise seed local heterogeneity during film formation. The $EDTA^{4-}$ incorporation not only promotes homogeneous nucleation but also controls crystallization kinetics through enhanced coordination ability, manifesting coherent and oriented growth in which chemical reconstruction of locally disordered lattice sites continuously suppresses surface HP defects and supports aligned HP lattices. As a result, these structural refinements homogenize the electronic landscape and suppress defect-associated band-tail states, mitigating non-radiative recombination losses and thereby improving PSC device performance. Our study highlights the importance of the coordination environment in the crystallization kinetics of solution-processed HPs and offers precursor-chemistry-based design guidelines for chelating additives that control crystal growth pathways to minimize defect formation and promote high-quality HP films.

2 | Results and Discussion

To regulate the coordination environment, EDTA was selected as a representative multidentate chelating agent with multiple carboxylic acid groups, enabling strong coordination with Pb^{2+} and allowing us to explore the effects of different deprotonation states on the coordination environment. Tuning the degree of EDTA deprotonation may provide a strategy to more precisely adjust the Pb—I coordination equilibria and iodoplumbate speciation in the precursor solution. Therefore, we selected EDTA additives with different deprotonation states ($EDTA^{2-}$ and $EDTA^{4-}$) to modulate the coordination environment of Pb^{2+} in the precursor solution. As the degree of EDTA deprotonation increases, both the negative charge density and the availability of carboxylate donor sites increase, which can strengthen Pb^{2+}–EDTA interactions and shift Pb—I coordination equilibria [33, 35, 36]. By modulating these equilibria, we aim to control iodoplumbate clusters that can act as prenucleation species and thereby influence nucleation and crystal growth, as schematically illustrated in Figure 1a.

To quantitatively evaluate the competitive coordination between EDTA additives and I^- ions for Pb^{2+} in the precursor solution, UV–vis absorption titration experiments were conducted (Figure S1). PbI_2 solutions containing different EDTA additives were titrated with formamidinium iodide (FAI), enabling us to monitor the evolution of Pb—I coordination under conditions relevant to HP precursor formation. As the concentration of I^- increases, the Pb—I coordination equilibrium shifts toward higher-order iodoplumbate complexes. This enables a comparison of how each EDTA additive modulates this equilibrium. The formation equilibrium constant (K_{eq}) describing this Pb—I interaction was extracted from absorption changes associated with iodoplumbate formation (Figure S2) using Benesi–Hildebrand analysis (Figure S3) [37, 38]. As shown in Figure 1b, the pristine solution exhibits the highest K_{eq} value, indicating a strong equilibrium toward

16163028, 2026, 49, Downloaded from https://advanced.onlinelibrary.wiley.com/doi/10.1002/adfm.75810 by Hanyang University Library, Wiley Online Library on [22/11/2026]. See the Terms and Conditions (https://onlinelibrary.wiley.com/terms-and-conditions) on Wiley Online Library for rules of use; OA articles are governed by the applicable Creative Commons License

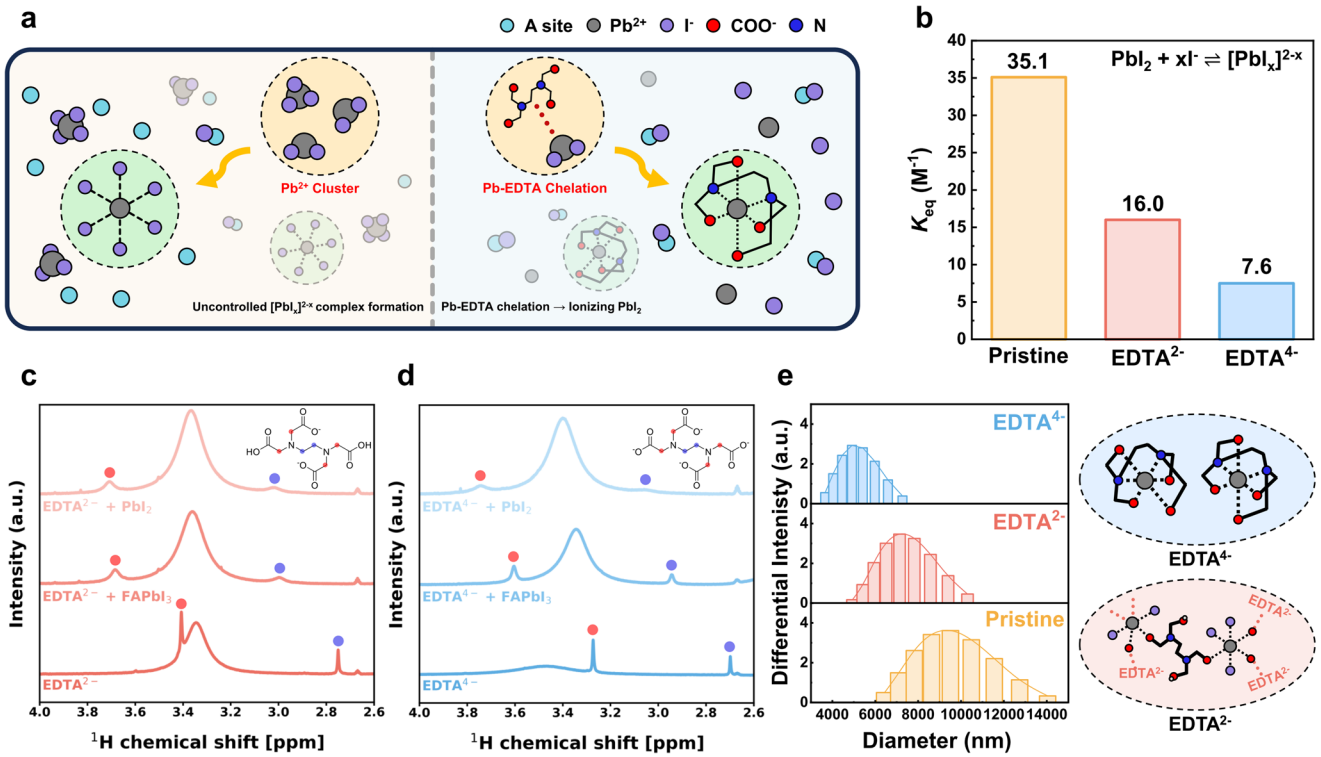

FIGURE 1 | (a) Schematic of HP and EDTA-salt-HP complex formation. (b) Equilibrium constant of PbI_2 and EDTA-salt + PbI_2 solution. (c,d) ^{1}H-NMR of EDTA additives and mixture solution (H_2O peak: ~ 3.38 ppm). (e) DLS data of the Pristine precursor solution and the solutions with respective EDTA additives.

higher-order iodoplumbate complexes. In contrast, the introduction of EDTA additives markedly suppressed Pb—I coordination, with fully deprotonated $EDTA^{4-}$ exhibiting the lowest K_{eq} value (pristine > $EDTA^{2-}$ > $EDTA^{4-}$). These results demonstrate that increasing chelation ability, which can be modulated by the deprotonation state of EDTA, enables EDTA to outcompete I^- for Pb^{2+} coordination and thereby suppress iodoplumbate formation in solution.

^{1}H Nuclear magnetic resonance (^{1}H-NMR) spectroscopy was employed to investigate the coordination behavior of EDTA additives in precursor solutions by comparing neat EDTA solutions with $FAPbI_3$, PbI_2, and FAI containing counterparts (Figure 1c,d and Figure S4). Both $EDTA^{2-}$ and $EDTA^{4-}$ exhibit clear downfield shifts of the methylene proton and ethylene proton resonance upon coordination with Pb^{2+}, indicating a collective redistribution of electron density across the EDTA framework. This behavior supports the involvement of both carboxylate oxygen and amine nitrogen donor sites in forming the coordination environment [39]. Moreover, the same downfield chemical shift is observed under both FAI and $FAPbI_3$ conditions, suggesting that the EDTA additives not only coordinate with Pb^{2+} but can also interact with FA^+. We note that a resonance at ~3.38 ppm is attributed to residual water in the DMSO-d_6 solvent, where its leverage in the overall precursor chemistry is deemed to be negligible.

To examine whether EDTA additives interact with A-site cations in solution, the FA^+ proton signal was analyzed using FAI and $FAPbI_3$-containing solutions (Figure S5) [5, 40, 41]. In the I-rich $FAPbI_3$ precursor solutions, both $EDTA^{2-}$ and $EDTA^{4-}$ show similar NH_2 splitting and CH multiplet features, suggesting that these spectral changes predominantly arise from the non-equivalent local electrostatic fields and ion-pairing configurations associated with iodoplumbate/I-rich environments rather than from site-specific EDTA–FA^+ association [42]. In contrast, the FAI-only mixtures show distinct behaviors for different EDTA species. $EDTA^{2-}$-FAI exhibits pronounced NH_2 splitting with CH multiplet signatures, consistent with non-averaged local interactions enabled by the coexistence of —COOH and —COO^- groups, whereas $EDTA^{4-}$-FAI shows an unsplit, downfield-shifted NH_2 resonance and a singlet CH signal, indicative of a dynamically averaged electrostatic environment due to rapid exchange in the uniformly deprotonated $EDTA^{4-}$ framework.

2D ^{1}H Nuclear Overhauser Effect Spectroscopy (NOESY) was further employed to investigate spatial proximity and interaction dynamics in the precursor solutions. In the $EDTA^{4-}$-$FAPbI_3$ solution, a distinct NOE cross-peak was observed between the methylene and ethylene protons of $EDTA^{4-}$, indicating that these protons are in close spatial proximity within the $EDTA^{4-}$ framework (Figure S6). This intramolecular NOE could suggest that $EDTA^{4-}$ can form a multidentate chelation to Pb^{2+} with a relatively constrained coordination geometry. In contrast, in the $EDTA^{2-}$-$FAPbI_3$ solution, no prominent intramolecular NOE cross-peak was detected within the $EDTA^{2-}$ (Figure S7). This result suggests that, due to partial protonation (coexistence of —COOH and —COO^-), $EDTA^{2-}$ may exhibit more dynamic coordination, leading to a lower degree of spatial constraint in Pb^{2+} chelation.

16163028, 2026, 49, Downloaded from https://advanced.onlinelibrary.wiley.com/doi/10.1002/adfm.75810 by Hanyang University Library, Wiley Online Library on [22/11/2026]. See the Terms and Conditions (https://onlinelibrary.wiley.com/terms-and-conditions) on Wiley Online Library for rules of use; OA articles are governed by the applicable Creative Commons License

Under FAI-only solutions, the exchange behavior of FA^+ differed markedly depending on the deprotonated state of EDTA. In the $EDTA^{4-}$-FAI solution, the FA^+ resonances were observed as singlets without splitting, and a strong exchange cross-peak appeared between the NH_2 protons of FA^+ and trace H_2O in the solvent (Figure S8). This cross-peak indicates an exchange-dominated environment in which NH_2 protons undergo rapid exchange with H_2O. Since $EDTA^{4-}$ contains uniformly deprotonated —COO^- groups, the electrostatic environment around FA^+ can be rapidly averaged, which can account for the simultaneous observation of singlet features and strong NH_2–H_2O exchange. Moreover, because FA^+ is bulkier than metal ions and imposes greater geometric constraints for multidentate binding, even if ionic association with $EDTA^{4-}$ occurs, it is more likely to exist as a partial-contact/ion-pair configuration rather than a fully encapsulated complex, thereby preserving sufficient accessibility for NH_2–H_2O exchange. In addition, the exchange component observed for NH_2–CH is more reasonably attributed to indirect magnetization transfer driven by rapid NH_2–H_2O exchange, rather than to direct NH_2–CH exchange [43, 44]. By contrast, in the $EDTA^{2-}$-FAI mixture, an exchange cross-peak was observed between the split NH_2 resonances of FA^+ (Figure S9), indicating that NH_2 protons undergo exchange between distinct local chemical environments.

These NMR results suggest that $EDTA^{2-}$ forms more complex and heterogeneous interaction networks with Pb^{2+} and FA^+ due to its non-uniform functional group environment arising from the coexistence of —COOH and —COO^-. In contrast, $EDTA^{4-}$ may establish more defined coordination/ion-pair environments through uniformly —COO^--based interactions and its tendency toward multidentate chelation with Pb^{2+}.

Dynamic light scattering (DLS) analysis was performed to evaluate how the coordination environments induced by the deprotonation state of EDTA influence the size and distribution of PbI_2-derived clusters in the precursor solution (Figure 1e). The pristine solution exhibits the largest average cluster size along with the broadest size distribution, reflecting the strong tendency of Pb—I species to form inhomogeneous aggregates in the absence of effective coordination control. Upon the addition of $EDTA^{2-}$, the overall cluster size is reduced compared to the pristine solution, indicating partial suppression of Pb—I aggregation. Although $EDTA^{2-}$ can coordinate with Pb^{2+}, its partially deprotonated state leads to a heterogeneous and dynamic coordination/ion-pairing environment, resulting in insufficient dissociation of PbI_2 aggregates. Consequently, Pb—I clusters are reduced relative to the pristine solution but remain large and broadly distributed, indicating only partial regulation. In contrast, the $EDTA^{4-}$ solution displays a pronounced reduction in cluster size, accompanied by a markedly narrower size distribution. The fully deprotonated $EDTA^{4-}$ establishes a robust and homogeneous coordination environment that stabilizes Pb^{2+} while maintaining FA^+ in a dynamically solvated state, thereby suppressing uncontrolled Pb—I association. As a result, the iodoplumbate clusters that act as prenucleation species remain small and narrowly distributed, preventing their overgrowth into inhomogeneous aggregates.

To gain insight into how the distinct binding ability of EDTA additives as a function of their deprotonated states impacts the early-stage crystallization behaviors, we implement a high-throughput automated experimental framework [45]. By using a pipetting robot, a microplate of HP precursors—$Cs_{0.15}FA_{0.85}PbI_3$ (denoted as CsFA) due to its crystallizing feasibility at low temperature [46–48]—with different concentrations of $EDTA^{4-}$ or $EDTA^{2-}$ in each well is prepared (Figure S10). Then, chloroform as an antisolvent was injected into precursor solutions, initiating the nucleation and the subsequent growth of the HP microcrystals. The resulting microplate is quickly transferred to the multimodal optical reader, and the photoluminescence (PL) spectra from all wells are collected over time (Figure S11), thereby monitoring the early-stage crystallization behaviors [45]. In this work, we focus on the temporal changes in PL peak wavelength and intensity, reflecting the kinetics of homogeneous crystal growth and their stability, respectively, as schematically described in Figure 2a.

Figure 2b shows the spectro-temporal PL map of the pristine CsFA HP microcrystals, synthesized by high-throughput robotic experimentation. The PL peak centered at ~795 nm, associated with the homogeneous $Cs_{0.15}FA_{0.85}PbI_3$, initially emerges [46, 47], which rapidly disappears within 30 min. This indicates that the CsFA HPs, despite the desired cation composition, are rapidly decomposed into the precursor state, which is likely due to the high density of the defects in the initial crystallites in the solid-solution mixture [49]. By introducing EDTA additives, the lifetime of the PL signals becomes drastically prolonged, involving progressive PL redshifts over time, as representatively shown in Figure 2c,d. Collectively, such features are obviously observed with increasing the additive concentrations, where the use of $EDTA^{2-}$ requires a higher concentration than the $EDTA^{4-}$ counterparts. The PL redshifts can be attributed to the defect-compensated growth (i.e., lattice coarsening) and promoted crystallization of FA-rich HP microcrystals from their precursor states [49], while the prolonged PL signal suggests that the later-formed HP phase has improved lattice stability as a result of EDTA additive incorporations (vide infra).

To comprehensively and quantitatively understand the large PL results obtained by the high-throughput experimentation, we integrate the LMFit-based analytic workflow into the overall experimental framework [50]. This allows us to automatically extract peak intensities and centers over time. Figure S12a,b shows the extracted time-evolution profiles of PL peak wavelengths for the CsFA HP microcrystals with varying $EDTA^{4-}$ or $EDTA^{2-}$ concentrations, respectively. For pristine HPs, the peak wavelength rapidly shifts from 795 to >840 nm within 30 min (highlighted as green lines in Figure S12), indicating that the antisolvent-induced crystallization occurs extremely fast. Note that, while LMFit can reliably capture the shift of PL peak center up to ~840 nm, the output over 840 nm from this analysis should be regarded as the disappearance of the corresponding PL spectra (i.e., misinterpreting the background noise), as the PL peak of pure α-$FAPbI_3$ appears <840 nm [51].

Incorporation of EDTA additives slows down the PL redshifts, which takes around 90 min to reach to ~835 nm. It is also noteworthy that, for all reaction reservoirs across the microplate, the PL intensities gradually decrease (Figure S13), indicating that the HP crystallites are unlikely be produced further over time during the crystallization. Given the dynamic growth nature of HPs, such marginal changes in peak wavelengths (particularly,

16163028, 2026, 49, Downloaded from https://advanced.onlinelibrary.wiley.com/doi/10.1002/adfm.75810 by Hanyang University Library, Wiley Online Library on [22/11/2026]. See the Terms and Conditions (https://onlinelibrary.wiley.com/terms-and-conditions) on Wiley Online Library for rules of use; OA articles are governed by the applicable Creative Commons License

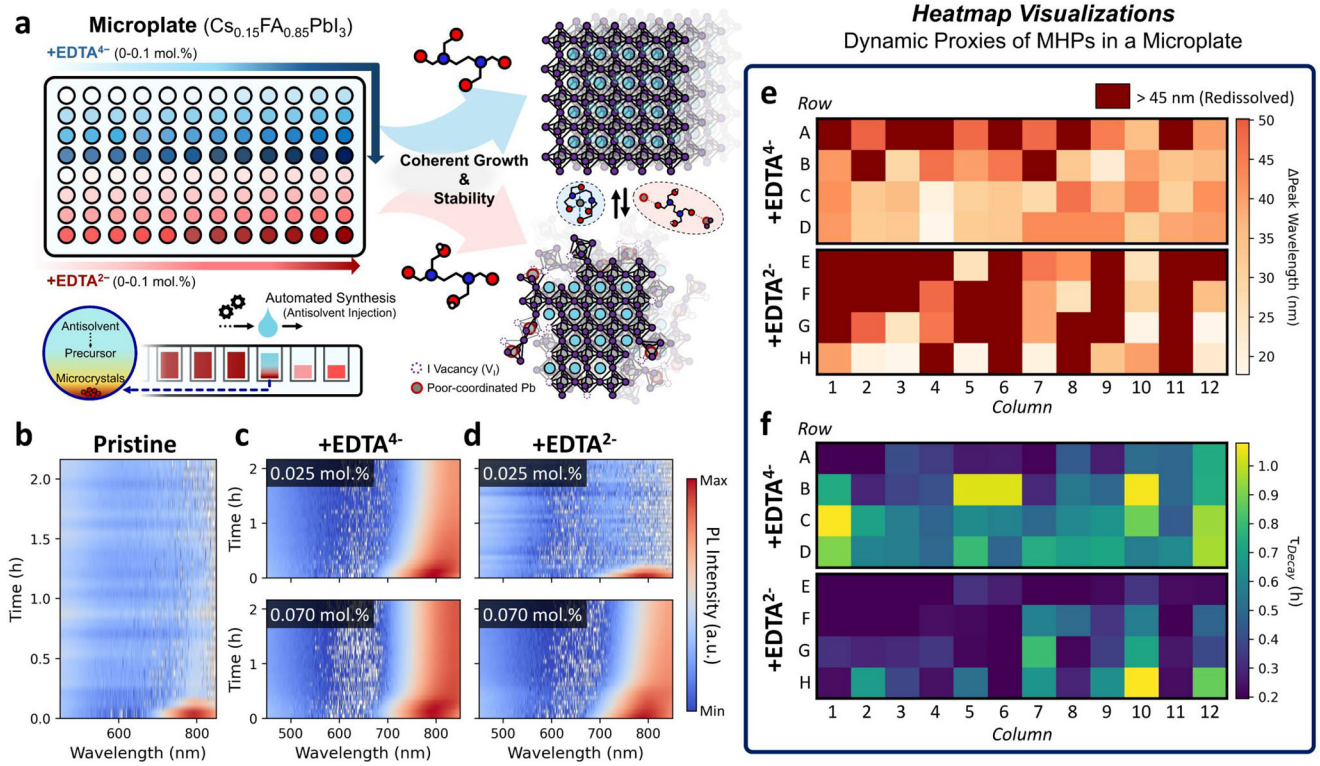

FIGURE 2 | (a) Schematic illustration describing high-throughput exploration of EDTA chemistry in HP crystallization dynamics. (b–d) Spectro-temporal maps of the CsFA HP microcrystals (b) without additives, with (c) $EDTA^{4-}$ and (d) $EDTA^{2-}$ additives (at two different concentrations), respectively. Heatmaps demonstrating (e) peak shifts within an hour and (f) decay times (τ_{Decay}) observed across the synthesized HP microplates, respectively.

within 30 min from antisolvent injection) and the simultaneous PL intensity drop collectively suggest that EDTA additives manifest the lattice coarsening process [49]. That is, rather than rapidly producing lots of HP microcrystals with considerable defect densities, EDTA additives likely promote the growth of the HP lattice while compensating for such defects. It has been found that the chelation effect of EDTA not only passivates the HP surface, but also acts as a Pb^{2+} scavenger to clean the cluttered surface [39]. In our study, while chelation of Pb^{2+} with EDTA can primarily disintegrate the bulk PbI_2 clusters and retard the HP crystallization, as speculated from the corresponding equilibrium constants (Figure 1b), the free EDTA ions, after releasing Pb^{2+}, can reorganize the HP lattice by re-taking the undercoordinated surface Pb^{2+} in the solution. During the crystallization, Pb^{2+} release and surface cleaning may contribute to the controlled growth of HP microcrystals with lower defect densities.

Over time, the peak wavelengths approach a saturation value of ~835 nm—corresponding to that of the pure α-$FAPbI_3$, likely due to the growth of $FAPbI_3$ after fully depletion of Cs^+ in the precursor solutions, which is easier to crystallize out due to the poor solubility [46, 47]. We note that it is impossible to sustain the black phase of HP microcrystals from pure $FAPbI_3$ precursors under similar conditions. Therefore, we hypothesize that the initially formed CsFA HP crystallites can serve as seeds for subsequent growth of the $FAPbI_3$-phase microcrystals taking place at this stage, hence promoting the coherent HP growth. Although this phase is unlikely to be observed from the spin-coated films due to the fast processing time, the PL dynamics of this phase in the high-throughput microcrystal experiments further offer insights into the influence of EDTA additives on the subsequent HP growth dynamics.

Figure 2e shows the heatmap visualization of the temporal PL peak shifts after an hour from antisolvent injection upon incorporation of $EDTA^{4-}$ or $EDTA^{2-}$ additives. Here, the wells exhibiting >45 nm of PL redshifts (i.e., peak wavelength >845 nm) are omitted. Given that the nucleation dynamics are mainly reflected within 30 min in the high-throughput experimentations, the heatmap showing the peak shifts during an hour implies how the coherent growth of the HP lattice can proceed. Key distinct behaviors are observed between the $EDTA^{4-}$ and $EDTA^{2-}$ systems. Upon $EDTA^{4-}$ incorporation, the HPs undergo moderate PL shifts of 10–30 nm, and the crystallites are retained across most of the concentration range. In contrast, the shifts become smaller (<20 nm) upon the $EDTA^{2-}$ addition, which also involves the notable PL disappearance (by redissolution) across the concentration range. This indicates that, during early-stage crystallization, $EDTA^{4-}$ can effectively regulate the defect density of the crystallites, thus quickly forming HP nuclei with clean surfaces, which favor the coherent growth of the HP lattice. While $EDTA^{2-}$ can chelate with Pb^{2+}, the geometrically imperfect binding nature of $EDTA^{2-}$ can impede the 'surface cleaning'. This, in turn, results in the formation of HP nuclei with residual atomically cluttered surfaces, which not only cause uneven crystal growth but also compromise the lattice stability.

16163028, 2026, 49, Downloaded from https://advanced.onlinelibrary.wiley.com/doi/10.1002/adfm.75810 by Hanyang University Library, Wiley Online Library on [22/11/2026]. See the Terms and Conditions (https://onlinelibrary.wiley.com/terms-and-conditions) on Wiley Online Library for rules of use; OA articles are governed by the applicable Creative Commons License

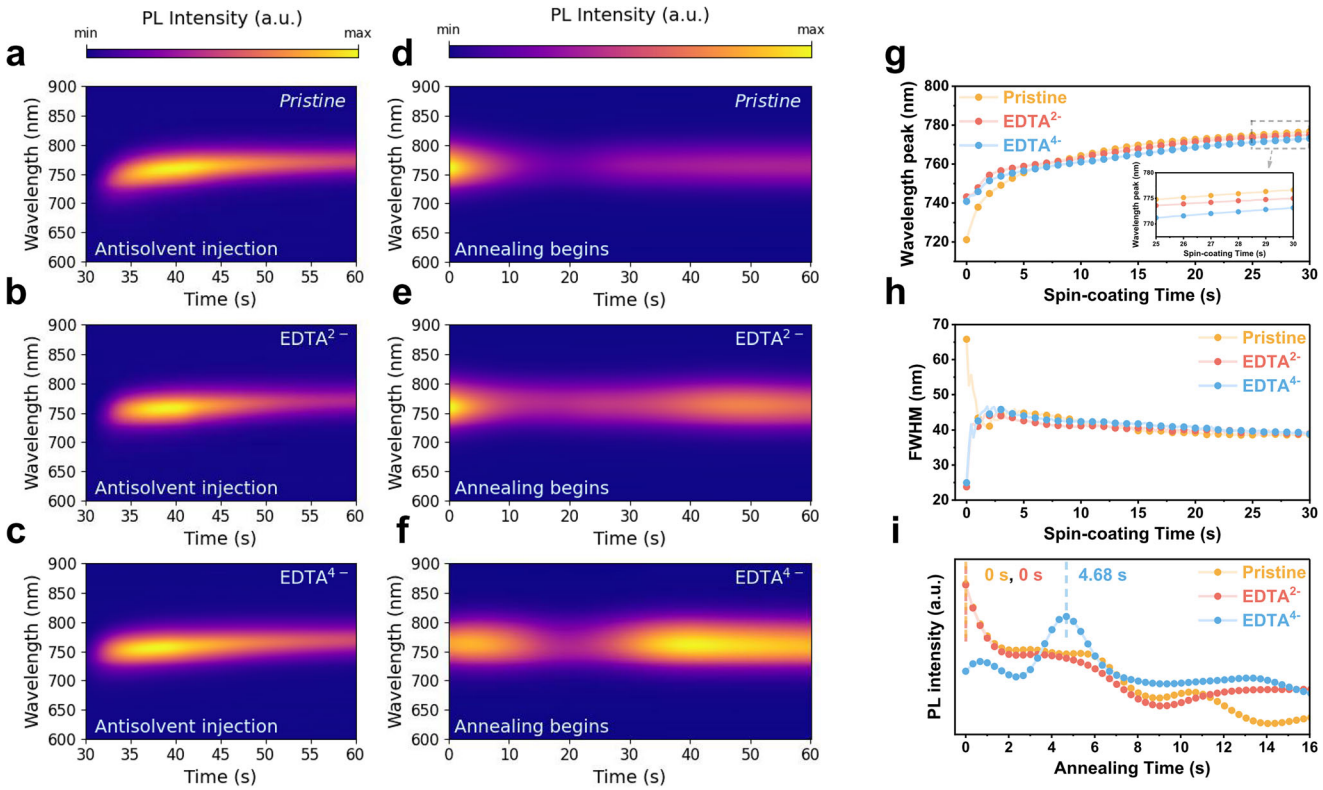

FIGURE 3 | (a–f) In situ PL spectra during (a–c) spin-coating and (d–f) annealing for pristine, $EDTA^{2-}$, and $EDTA^{4-}$ HP films. (g–i) the extracted values of (g) wavelength peak, (h) FWHM, and (i) PL intensity from the in situ PL measurements, performed on glass/perovskite structures with excitation and PL collection from the top side of the perovskite film.

To gain more insights into the crystallization dynamics and lattice stability, the extracted PL intensity profiles—all showing the decreasing trends—are fitted with a monoexponential decay model, and the PL decay time (τ_{Decay}) for each well in the microplate is estimated (Figure S14). These values are also visualized as a heatmap in Figure 2f, indeed showing a strong correlation between the PL redshifts (Figure 2e) and the longer τ_{Decay}. Specifically, the longer τ_{Decay}, the larger peak shifts. Also, the incorporation of $EDTA^{4-}$ offers longer τ_{Decay} and greater peak shifts compared to $EDTA^{2-}$ counterparts. These observations indicate that the slow crystallization dynamics—mirrored as slow PL decay—indeed benefits the coherent lattice growth, where the complete coordination of $EDTA^{4-}$ outperforms $EDTA^{2-}$. Furthermore, the HP microcrystals synthesized with $EDTA^{4-}$ exhibit excellent lattice stability in the solid-precursor solution mixture, whereas most of those with $EDTA^{2-}$ undergo complete redissolution over time (Figure S15). This observation further suggests that HP lattices formed with $EDTA^{4-}$ incorporation, characterized by slow crystallization, can promote coherent lattice growth with minimized defects as well as enhanced lattice stability.

Having explored the high-throughput insights into the macroscopic crystallization dynamics, we now focus on elucidating how the chelation behavior of the EDTA additive regulates crystallization kinetics under practical film deposition. To this end, in situ photoluminescence (PL) measurements were performed throughout the spin-coating (Figure 3a–c) and subsequent annealing processes (Figure 3d–f). Distinct PL differences between the pristine and EDTA-incorporated films appear immediately after anti-solvent injection during spin-coating. The pristine film shows PL onset at ~720 nm, followed by a rapid redshift of the PL peak to ~770 nm with time (Figure 3g). It also exhibits a very broad initial full width at half maximum (FWHM, ~65 nm), indicating highly inhomogeneous and disordered nucleation occurring (Figure 3h). In contrast, EDTA additives incorporated films exhibit initial PL at longer wavelength (~740 nm) with a narrow FWHM (~25 nm) and show a relatively gradual shift of the PL peak over time. These results suggest that, in the pristine film, uncontrolled clusters trigger indiscriminate nucleation, whereas Pb^{2+} chelation by EDTA additives suppresses disordered aggregation and promotes a more regulated, homogeneous nucleation pathway. Notably, at the end of spin-coating, the PL peak positions follow the order pristine > $EDTA^{2-}$ > $EDTA^{4-}$, indicating that $EDTA^{4-}$ more effectively regulates Pb^{2+} coordination equilibria and precursor-cluster dynamics through a stronger and homogeneous coordination environment, thereby promoting a more homogeneous nucleation pathway. This suppresses the formation of large iodoplumbate aggregates and instead promotes a more uniform distribution of smaller precursor clusters. Consistent with this interpretation, the time-resolved PL intensity evolution (Figure S16) reveals that the $EDTA^{4-}$ film exhibits the earliest increase in PL intensity, indicating an earlier nucleation onset compared to the pristine and $EDTA^{2-}$ films. Together with the PL peak evolution and FWHM analysis (Figure 3g,h), these results support that $EDTA^{4-}$ induces a more homogeneous nucleation pathway, enabling earlier formation of high-quality perovskite nuclei. Meanwhile, to examine the influence of the counter alkali-metal cations in the EDTA salts, we measured the in situ PL evolution and the optical properties of the resulting films. No

16163028, 2026, 49, Downloaded from https://advanced.onlinelibrary.wiley.com/doi/10.1002/adfm.75810 by Hanyang University Library, Wiley Online Library on [22/11/2026]. See the Terms and Conditions (https://onlinelibrary.wiley.com/terms-and-conditions) on Wiley Online Library for rules of use; OA articles are governed by the applicable Creative Commons License

significant differences were observed relative to the pristine film, suggesting that the crystallization control primarily originates from the EDTA additive itself rather than from the counter cations (Figures S17 and S18).

To further probe crystal growth kinetics following spin-coating, the temporal evolution of PL intensity was monitored during the subsequent annealing process (Figure 3d–f). A transient decrease in PL intensity is observed at ~20 s, which is attributed to structural rearrangement or phase transition during annealing, where intermediate to perovskite phase evolution and compositional redistribution can temporarily enhance non-radiative recombination, leading to PL quenching [52, 53]. The PL intensity then gradually recovers as the perovskite lattice becomes more stabilized. As shown in Figure 3i, both the pristine and $EDTA^{2-}$ films exhibit a maximum PL intensity at the onset of annealing (0 s), suggesting that rapid crystal growth has already occurred at the very early stage of annealing, within a timescale shorter than the temporal resolution of the in situ PL measurement. In contrast, the $EDTA^{4-}$ film exhibits a delayed evolution of PL intensity, reaching a maximum at 4.68 s after annealing begins. This delayed PL-intensity maximum indicates slower crystallization kinetics induced by strong Pb^{2+}-$EDTA^{4-}$ chelation [52, 53]. Therefore, the analysis focuses on the initial stage of annealing (0–16 s), where nucleation and early crystal growth predominantly occur, and the differences in crystallization kinetics are most clearly resolved.

In the pristine film, the absence of effective chemical regulation in the precursor solution leads to uncontrolled inhomogeneous nucleation, which can affect rapid and spatially non-uniform crystal growth during subsequent film deposition. $EDTA^{2-}$ can mitigate excessive aggregation through moderate chelation with Pb^{2+}. However, due to limitations in coordination strength and inhomogeneous coordination environment, it may not sufficiently resolve precursor cluster inhomogeneity, potentially restricting nucleation and growth control. In contrast, the fully deprotonated $EDTA^{4-}$, supported by strong and more homogeneous coordination with Pb^{2+}, more effectively regulates cluster dynamics, thereby delaying nucleation and early growth and providing a more homogeneous growth environment [54]. This kinetic regulation can offer sufficient time for surface cleaning during crystallization, in which $EDTA^{4-}$ repeatedly binds to and dissociates from uncoordinated Pb^{2+} at the defective lattice, thereby promoting defect suppression while supporting coherent lattice growth.

Grazing-incidence wide-angle X-ray scattering (GIWAXS) measurements were performed to investigate how chelation-controlled crystallization influences the crystallographic structure and phase distribution of the resulting HP films. The incident angle (α_i) was varied from 0.05° to 0.50° to obtain depth-resolved structural information from the film surface to the bulk region (Figures S19–S21). The GIWAXS patterns confirm that all films exhibit the characteristic HP diffraction features, indicating successful HP phase formation regardless of additive incorporation (Figure 4a–f). However, pronounced differences in the ring pattern were observed depending on impurity phases, suggesting distinct crystallization pathways governed by precursor chemistry. In the pristine film, an additional diffraction feature at $q \approx 0.90$ Å^{-1}, assigned to PbI_2, is consistently observed across all incident angles, indicating the persistence of residual PbI_2 within the HP matrix (Figure 4d). In the $EDTA^{2-}$ film, the PbI_2-related feature is largely suppressed; however, a new diffraction peak emerges around 0.8–0.95 Å^{-1} in the bulk region, which can be attributed to non-perovskite hexagonal polytype phases (Figure 4e) [55]. This may suggest that the rapid crystallization in the $EDTA^{2-}$ case, together with a heterogeneous coordination environment between Pb^{2+} and FA^+, could contribute to stabilizing the hexagonal polytype phase [56]. By contrast, the $EDTA^{4-}$ film exhibits only the α-phase HP diffraction peaks without any impurity phases over the entire range of incident angles (Figure 4f). This phase homogeneity is attributed to the stronger and more effective chelation provided by the fully deprotonated $EDTA^{4-}$, indicating that both crystallization kinetics and the coordination environment are critical for achieving phase purity.

Building on the phase analysis above, the influence of chelation-controlled crystallization on lattice characteristics was further evaluated through *d*spacing analysis of the HP (100) peak located near $q \approx 1.00$ Å^{-1} (Figure 4g). Gaussian fitting was applied to extract peak positions, and the corresponding lattice spacing was calculated using Bragg's relation ($q = 2\pi/d$). The pristine film exhibits comparatively smaller d-spacing values across the incident angle range, with the largest deviation between near-surface-probed and bulk-probed conditions, suggesting the presence of internal lattice strain associated with rapid and non-equilibrium crystallization [57, 58]. In contrast, the $EDTA^{4-}$ incorporated film shows slightly expanded d-spacing and a reduced incident-angle dependence, indicative of a more relaxed lattice configuration enabled by kinetically controlled crystal growth. These observations suggest that the slow crystal growth induced by strong chelation facilitates relaxation of residual lattice strain that typically occurs in rapid crystallization.

Figure 4h summarizes the full width at half maximum (FWHM) values extracted from azimuthal integration of the HP (100) peak at different incident angles, providing a quantitative assessment of crystallographic orientation (Figures S22–S24). The pristine film exhibits the largest FWHM values, indicating substantial orientational disorder. Upon incorporation of EDTA additives, the FWHM values decrease with $EDTA^{2-}$ exhibiting a moderate reduction and $EDTA^{4-}$ showing the lowest FWHM across the entire incident angle range. This trend indicates that increasing the degree of EDTA deprotonation leads to improvement in orientational uniformity. Nevertheless, the FWHM of the (100) peak alone does not fully describe the nature of preferred crystallographic orientation. Notably, although the (100) plane is suitable for evaluating relative orientational disorder, its azimuthal peak position in triple-cation perovskite systems typically appears near ~40°, rather than at 90°, as reported previously [59]. This behavior arises from the compositional complexity of triple-cation HPs, in which mixed A-site cations stabilize a distorted cubic lattice and alter the relative surface energies of low-index facets [59, 60]. Consequently, the (100) plane might not be ideal for directly identifying the preferred out-of-plane orientation relative to the substrate. Therefore, to unambiguously determine the preferred crystallographic orientation along the out-of-plane direction, the azimuthal intensity distribution of the (111) peak was analyzed (Figure S25). In contrast to the (100) plane, the (111) plane exhibits a well-defined azimuthal peak centered near 90°, corresponding to an out-of-plane alignment. Note that the

16163028, 2026, 49, Downloaded from https://advanced.onlinelibrary.wiley.com/doi/10.1002/adfm.75810 by Hanyang University Library, Wiley Online Library on [22/11/2026]. See the Terms and Conditions (https://onlinelibrary.wiley.com/terms-and-conditions) on Wiley Online Library for rules of use; OA articles are governed by the applicable Creative Commons License

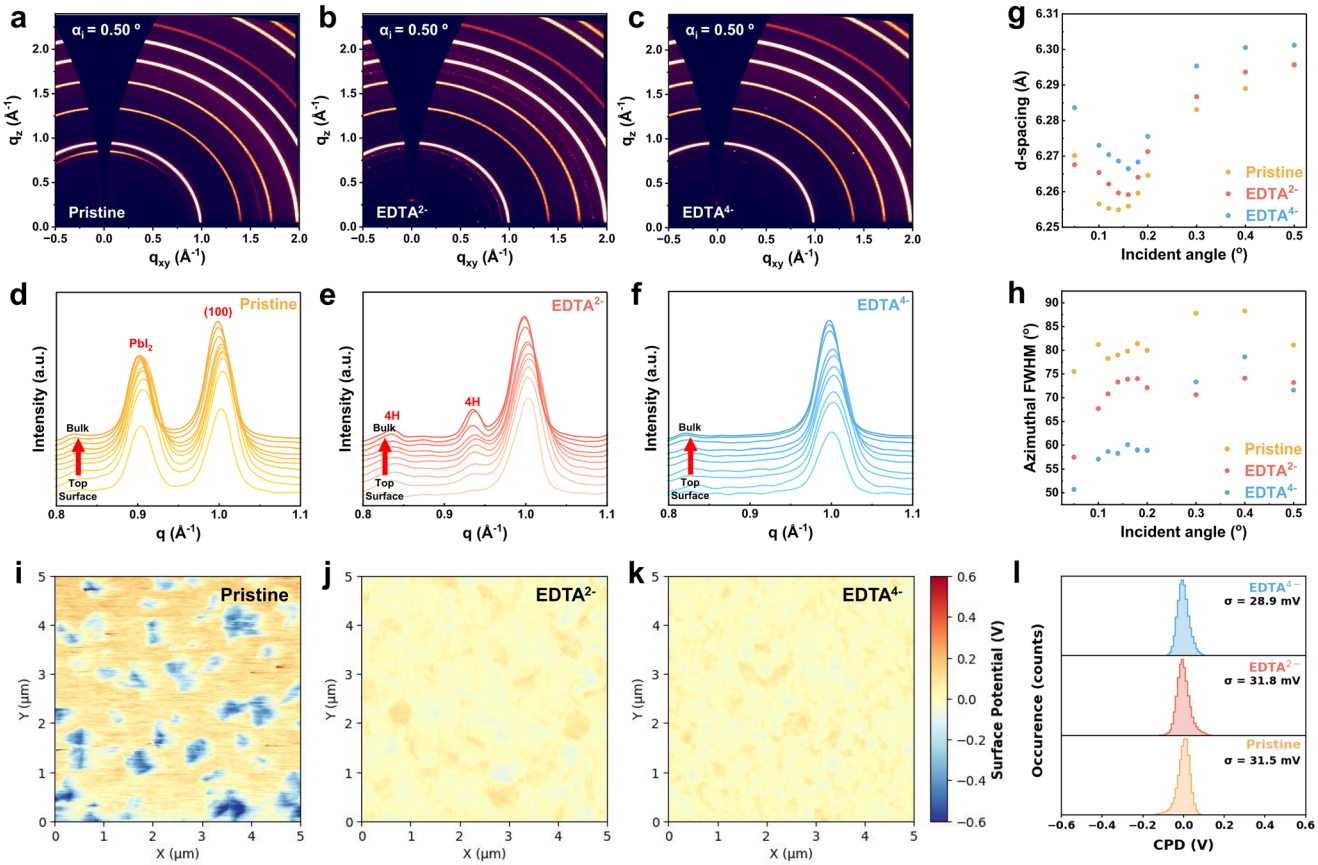

FIGURE 4 | (a–c) 2D GIWAXS patterns of the (a) pristine and (b,c) HP films at an incident angle of 0.50°. (d–f) Azimuthally integrated intensity profiles derived from the GIWAXS patterns of the (d) pristine and (e,f) EDTA-incorporated films with the incident angle from 0.05° to 0.50° in 0.1° increments. (g) Azimuthal intensity integrations at an incident angle of the pristine HP (100) phase with the incident angle from 0.05° to 0.50°. (h) *d*-spacing value at an incident angle of the pristine HP (100) films with the incident angle from 0.05° to 0.50°. (i–k) KPFM images of (i) pristine and (j,k) EDTA-incorporated films. (l) KPFM histogram of pristine and EDTA-incorporated films.

$EDTA^{4-}$ incorporated film displays a sharp and narrow azimuthal peak at 90°, whereas the pristine and $EDTA^{2-}$ incorporated films show much broader intensity distributions. Furthermore, during crystallization, free EDTA ions may induce facet-specific interactions at the surface, which could further favor crystal growth along the (111) orientation [60–63].

The influence of kinetically controlled crystallization on film morphology was further examined using atomic force microscopy (AFM) and scanning electron microscopy (SEM) (Figures S26–S28). AFM topography images (Figure S26) indicate that films incorporating EDTA additives exhibit more homogeneous surface features compared to the pristine film, despite no significant change in apparent grain size. Consistent with these observations, SEM images (Figure S27) show that films incorporating EDTA additives form a dense and continuous grain network. In contrast, the pristine film exhibits distinct regions with higher electron contrast related to residual PbI_2, consistent with the GIWAXS pattern. Furthermore, cross-sectional SEM images (Figure S28) demonstrate that the $EDTA^{4-}$ film develops a pronounced columnar grain structure extending across the entire film thickness. This structural feature indicates that controlled crystallization improves phase and structural homogeneity across the film. Such vertically coherent grain architecture is favorable for charge transport along the vertical direction of the device.

The impact of the observed structural improvements on the electronic properties was examined using Kelvin probe force microscopy (KPFM) mapping (Figure 4i–k). The pristine film exhibits pronounced spatial non-uniformity in surface potential, which is attributed to phase inhomogeneity arising from residual PbI_2. Such phase inhomogeneity introduces a disordered energetic landscape with locally distinct electronic environments, which can promote charge trapping and recombination. In contrast, films incorporating EDTA additives exhibit noticeably homogeneous potential distributions. Furthermore, as shown in Figure 4l, CPD histograms from KPFM images show a narrower distribution for the $EDTA^{4-}$ incorporated film compared to both the pristine and $EDTA^{2-}$ counterparts, indicating reduced surface potential distribution. This result aligns with the improved structural homogeneity revealed by GIWAXS, supporting that controlling crystallization kinetics is critical for establishing a smoother energetic landscape. The resulting electronic uniformity can mitigate barriers to charge transport/extraction and reduce recombination losses, thereby contributing to improved performance and stability of the device [64].

To gain more insights into the phase homogeneity of HP matrices at the macroscopic scale, PL intensity maps of the HP films are collected via PL microscopy. Figure S29a shows the PL intensity maps of the pristine HP film, exhibiting island-like local variation

16163028, 2026, 49, Downloaded from https://advanced.onlinelibrary.wiley.com/doi/10.1002/adfm.75810 by Hanyang University Library, Wiley Online Library on [22/11/2026]. See the Terms and Conditions (https://onlinelibrary.wiley.com/terms-and-conditions) on Wiley Online Library for rules of use; OA articles are governed by the applicable Creative Commons License

of PL intensities. In contrast, the corresponding PL maps of $EDTA^{2-}$ and $EDTA^{4-}$ films exhibit comparatively conformal PL intensities (Figure S29b,c). These observations confirm that EDTA incorporation indeed homogenizes the phase and energetics across the HP matrices on a macroscale, consistent with the nanoscopic observations by KPFM analysis. Specifically, dark spots are prevalent in the HP film incorporating $EDTA^{2-}$, likely attributed to the emergence of photo-inactive, non-perovskite δ-phases as seen in GIWAXS characterizations. Summarizing, PL mapping results exhibit consistent trends observed from GIWAXS and KPFM results, clearly supporting our hypothesis that the regulated crystallization kinetics of HPs with fully deprotonated $EDTA^{4-}$, achieved by its strong chelation, indeed manifests the phase-homogeneous macroscopic ensemble.

To probe the depth-dependent distribution of EDTA within the HP films, Time-of-flight secondary ion mass spectrometry (ToF-SIMS) depth profiling was performed. Figure S30 shows the depth profiles of negative ion signals for pristine, $EDTA^{2-}$-, and $EDTA^{4-}$-incorporated HP films. Whereas only HP-related signals are observed in the pristine film (Figure S30a), the EDTA-derived fragment $C_2H_3O_2^-$ is detected only in the $EDTA^{2-}$ and $EDTA^{4-}$ films, confirming the presence of EDTA (Figure S30b,c) [65]. These EDTA-related signals are relatively weak near the top region of the film but become more pronounced toward the buried interface with the underlying MeO-2PACz/ITO substrate. This suggests that, rather than being incorporated into the lattice, EDTA regulates Pb^{2+} coordination during the top-to-bottom crystallization process driven by solvent evaporation and antisolvent treatment and may subsequently contribute to local lattice rearrangement and defect suppression by transiently binding to uncoordinated Pb^{2+} at defective growth sites, before ultimately remaining near the lower interface or grain-boundary regions. These results are consistent with the proposed role of EDTA as a non-lattice component involved in crystallization control and surface cleaning during film formation.

Following the structural and electronic landscape analysis, UV–vis absorption spectroscopy was employed to assess the optical response of the HP films (Figure S31). To evaluate the optical bandgap and its correlation with structural disorder, Tauc plot analysis was performed based on the UV–vis absorption spectra (Figure S32) [50]. The optical bandgaps are estimated to be ~1.54 eV for the pristine and $EDTA^{2-}$ films, and ~1.52 eV for the $EDTA^{4-}$ film, obtained by extrapolating the linear region of the absorption edge. From the same analysis, the Urbach energy (E_u) was extracted to quantify the degree of electronic disorder. The pristine film exhibits the highest E_u value (23.7 meV), indicative of pronounced energetic disorder and a high density of band-tail states. The $EDTA^{2-}$ film shows a moderately reduced E_u (20.2 meV), while the $EDTA^{4-}$ film displays the lowest E_u value (19.9 meV). This progressive reduction in Urbach energy is consistent with the improved structural integrity and phase homogeneity achieved by $EDTA^{4-}$, indicating suppressed band-tail formation and reduced non-radiative recombination that are expected to enhance open-circuit voltage (V_{OC}) upon PSC applications.

Figure 5a,b schematically summarizes how crystallization kinetics regulated by EDTA additives govern the structural evolution of HP films. In the pristine system, insufficient regulation of the coordination environment leads to the persistence of poorly dissociated iodoplumbate clusters in the precursor solution, which promotes indiscriminate nucleation and growth under rapid kinetics (Figure 5a). During crystallization, clustered building blocks attach in a disordered manner, resulting in randomly oriented crystallites, residual PbI_2 domains, and accumulated lattice strain. Such growth behavior is accompanied by a high density of surface and interfacial defects, producing a strongly inhomogeneous energetic landscape across the film.

By contrast, incorporation of $EDTA^{4-}$ imposes effective coordination control at the precursor level (Figure 5b). Strong and chemically homogeneous multidentate chelation disassembles iodoplumbate clusters, suppressing uncontrolled prenucleation and steering crystallization onto a slower and more regulated pathway. The growth process proceeds through homogeneous nucleation followed by coherent lattice coarsening, supported by the distribution of uniform growth units (i.e., discrete Pb—I complexes) and the continuous maintenance of solution-solid interfacial equilibrium. By slowing early crystallization, this regulation provides sufficient time for surface cleaning during growth. As Pb^{2+} is incorporated into the lattice, EDTA is released and can transiently bind uncoordinated Pb^{2+} at defective surface sites, scavenging these defective sites and preventing their accumulation at the growth front. These effects enable continued lattice rearrangement and defect compensation, promoting improved crystallographic ordering with reduced lattice strain and suppressed impurity phase formation. As a result, EDTA chelation-controlled crystallization refined the film by minimizing structural and interfacial disorder, leading to a more homogeneous energetic landscape across the HP film.

To assess how the chelation-controlled crystallization control impacts practical device performance, the device characteristics of PSC devices incorporating EDTA additives were evaluated using inverted p-i-n devices with the architecture $FTO/4PADCB/Cs_{0.05}MA_{0.05}FA_{0.90}Pb(I_{0.95}Br_{0.05})_3/C_{60}/BCP/Ag$. Figure 5c presents the current density–voltage (*J-V*) charac teristics of the best-performing devices together with the statistical distribution of the V_{OC}. The incorporation of EDTA additives leads to distinctly different performance trends depending on their chelating ability. The $EDTA^{4-}$-based device exhibits the highest power conversion efficiency (PCE) of 26.37% with a V_{OC} of 1.19 V. By comparison, the $EDTA^{2-}$-incorporated device shows a lower PCE of 25.67% and a V_{OC} of 1.18 V, which is inferior to that of the pristine control device (PCE = 25.72%, V_{OC} = 1.17 V). Detailed device parameters for champion devices and statistical averages are summarized in Table S1. The enhanced performance of the $EDTA^{4-}$-incorporated device is attributed to chelation-controlled crystallization that promotes homogeneous nucleation and coherent lattice coarsening. This regulated crystallization enables surface cleaning and lattice rearrangement, thereby suppressing defect-assisted non-radiative recombination and leading to the higher V_{OC}.

By contrast, the inferior performance of the $EDTA^{2-}$-incorporated device is associated with its inhomogeneous coordination environment. While $EDTA^{2-}$ can suppress iodoplumbate clustering, its partially protonated mixed —COOH/—COO^- functionality imposes an inhomogeneous coordination environment and inconsistent regulation of prenucleation and early growth across the film, thereby enabling the formation of non-perovskite

16163028, 2026, 49, Downloaded from https://advanced.onlinelibrary.wiley.com/doi/10.1002/adfm.75810 by Hanyang University Library, Wiley Online Library on [22/11/2026]. See the Terms and Conditions (https://onlinelibrary.wiley.com/terms-and-conditions) on Wiley Online Library for rules of use; OA articles are governed by the applicable Creative Commons License

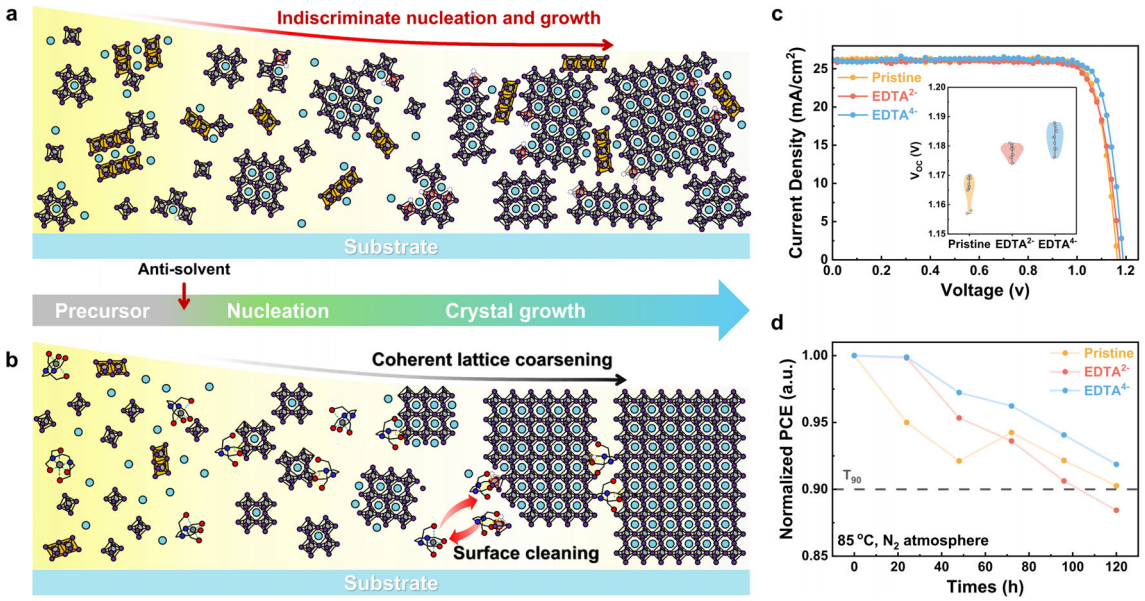

FIGURE 5 | (a,b) Schematics illustrating the crystallization process of (a) pristine and (b) the effect of $EDTA^{4-}$ on HP film formation. (c) *J–V* curves of PSCs. (d) Thermal stability profiles of PSCs based on pristine, $EDTA^{2-}$, and $EDTA^{4-}$ modified films. Thermal stability evaluated at 85°C in a N_2 atmosphere. The dashed lines indicate 90% of the initial power conversion efficiency (T_{90}).

hexagonal polytype during film formation. The persistence of these hexagonal polytype is more detrimental than residual PbI_2, as they form structurally mismatched heterointerfaces within the HP lattice. Such interfaces disrupt charge transport continuity and serve as preferential sites for non-radiative recombination, increasing recombination losses and reducing device efficiency [66, 67].

The inset of Figure 5c shows that devices incorporating EDTA additives exhibit statistically higher V_{OC} than the pristine devices, highlighting the effectiveness of chelation-controlled crystallization. Statistical distributions of all device parameters are provided in Figure S33. Consistent J_{SC} values obtained from *J–V* curves and integrated external quantum efficiency (EQE) spectra (Figure S34) confirm the reliability of the measurements. To gain further insight into the recombination dynamics associated with the enhanced V_{OC}, light-intensity-dependent V_{OC} measurements were conducted (Figure S35). The $EDTA^{4-}$-incorporated device exhibits a lower ideality factor ($n = 1.43$) compared to the pristine ($n = 1.45$) and $EDTA^{2-}$ ($n = 1.50$) devices, indicating reduced trap-assisted recombination. This result provides evidence that the improved phase homogeneity and controlled crystallization induced by $EDTA^{4-}$ effectively suppress defect-mediated recombination losses, contributing to the enhanced V_{OC} and overall device performance. In contrast, the higher ideality factor observed for the $EDTA^{2-}$ device suggests increased non-radiative recombination, likely associated with the formation of photoinactive non-perovskite δ-phases, which act as recombination centers and promote trap-assisted recombination. Accordingly, devices incorporating $EDTA^{4-}$ exhibit higher V_{OC}, underscoring the close linkage between crystallization kinetics control and device performance.

In addition, as shown in Figure 5d, the $EDTA^{4-}$-incorporated device exhibited the best thermal stability at 85°C in N_2. This behavior is attributed to the more effective crystallization control induced by $EDTA^{4-}$, which leads to improved phase homogeneity, reduced structural disorder, and suppressed formation of defect-rich regions and impurity phases, thereby yielding a thermally more stable HP matrix. By contrast, the pristine and $EDTA^{2-}$-incorporated devices showed relatively poorer thermal stability. In particular, the lower thermal stability of the $EDTA^{2-}$-incorporated device can be associated with the persistence of residual structural heterogeneity and non-perovskite hexagonal polytypes, which can act as vulnerable sites for degradation under thermal stress [15, 68]. The lower density of defect-mediated recombination centers likely mitigates degradation under thermal stress, thereby contributing to improved device stability.

3 | Conclusions

In summary, we investigated how chelate coordination chemistry in the precursor solution influences the crystallization behavior of HPs. We identified the deprotonation state of EDTA as a critical factor that defines the uniformity of the coordination environment in precursor solution, thereby setting the size and distribution of clustered iodoplumbate aggregates and the extent of crystallization kinetic control during film formation. We utilized a high-throughput microplate platform to quantify early-stage crystallization behavior by tracking time-resolved PL across a broad additive-concentration space. We also monitored in situ PL during practical film deposition to evaluate how the precursor coordination environment influences the crystallization pathway. Fully deprotonated $EDTA^{4-}$ forms rigorous and spatially uniform multidentate chelation that can neatly surround Pb^{2+} and A-site cations, thereby suppressing cluster-driven, indiscriminate nucleation and growth and instead promoting homogeneous nucleation followed by coherent lattice coarsening. Slowed crystallization provides sufficient time for in-process structural refinement, where EDTA released upon Pb^{2+}

16163028, 2026, 49, Downloaded from https://advanced.onlinelibrary.wiley.com/doi/10.1002/adfm.75810 by Hanyang University Library, Wiley Online Library on [22/11/2026]. See the Terms and Conditions (https://onlinelibrary.wiley.com/terms-and-conditions) on Wiley Online Library for rules of use; OA articles are governed by the applicable Creative Commons License

incorporation transiently binds uncoordinated Pb^{2+} at defective growth, driving chemical reconstruction of locally disordered lattice sites that cleans and suppresses surface HP defects as crystallization proceeds. As a result, $EDTA^{4-}$ incorporation refines the HP film into a coherently ordered matrix with preferred orientation, reduced lattice strain, suppressed impurity-phase formation, and a more homogeneous energetic landscape, consequently improving device performance. Our work highlights deprotonation-state engineering of chelating additives as a chemically intuitive strategy to tune precursor coordination environment and guide crystallization toward uniform, defect-suppressed HP films, with strong promise to bridge coordination chemistry and practical processing, delivering scalable fabrication with enhanced batch-to-batch reproducibility for commercialization.

4 | Experimental Section

4.1 | Materials

Formamidinium iodide (FAI; Greatcell solar, >99.99%), lead (II) iodide (PbI_2; Sigma–Aldrich), methylammonium bromide (MABr; Greatcell solar, >99.99%), lead (II) bromide ($PbBr_2$; thermos scientific, 98+%), cesium iodide (CsI; Sigma–Aldrich, 99.99%), methylammonium chloride (MACl; Greatcell solar, >99.99%), ethylenediaminetetraacetic acid dipotassium salt dihydrate ($EDTA^{2-}$; Sigma–Aldrich, ≥ 98%), ethylenediaminetetraacetic acid tetrasodium salt dihydrate ($EDTA^{4-}$; Sigma–Aldrich, 99.0%–102.0%), 1,3-diammoniumpropane diiodide ($PDAI_2$; TCI, 98.0%), *N*,*N*-dimethylformamide (DMF; Sigma–Aldrich, 99.8%), dimethyl sulfoxide (DMSO; Sigma–Aldrich, 99.5%), chlorobenzene (CB; Sigma–Aldrich, 99.8%), 2-methoxyethanol (2-ME; Sigma–Aldrich, anhydrous 99.8%), diethyl ether (DE; Sigma–Aldrich, ≥ 99.7%), ethanol (Sigma–Aldrich, ≥99.5%), 2-propanol (IPA; Sigma–Adrich, 99.5%), ethyl acetate (EA; Sigma–Aldrich, ≥ 99.5%), [2-(3,6-Dimethoxy-9*H*-carbazol-9-yl)ethyl]phosphonic Acid (MeO-2PACz; TCI, >98.0%), [4-(7*H*-Dibenzo[c, g]carbazole-7-yl)butyl]phosphonic Acid (4PADCB; TCI, >98.0%), fullerene (C_{60}; OSM, >99.5%), bathocuproine (BCP; OSM, >99.9%), Ag (iTASCO, 99.9%) were purchased and used without further purification.

4.2 | Solution Preparation (for High-Throughput Automated Experimentations)

4.2.1 | Preparation of $Cs_{0.15}FA_{0.85}PbI_3$ Precursor

All solution preparation steps were carried out inside an N_2-filled glovebox. A $Cs_{0.15}FA_{0.85}PbI_3$ precursor solution (1.25 M) was prepared by dissolving CsI, FAI, and PbI_2 (molar ratio = 0.15:0.85:1) in solvent (DMF:DMSO = 3:1 (v/v)).

4.2.2 | Preparation of EDTA Additive Solutions

Stock solutions of EDTA additives ($EDTA^{4-}$ and $EDTA^{2-}$) (5 mM) were prepared by dissolving each salt in solvent (DMF:DMSO = 3:1 (v/v)) and stirring for ~12 h at room temperature to ensure complete dissolution and homogenization prior to use.

4.3 | High-Throughput Automated Synthesis and Characterizations

The precursor solutions and other required chemicals were transferred to a pipetting robot system (Opentrons, OT-2) in an N_2-filled glovebox. First, for each well, 40 µL of the precursor solution was dispensed using a P300 single-channel pipette. Subsequently, stock solutions of two EDTA additives were added using a P20 single-channel pipette in amounts corresponding to the well-specific EDTA loading (0–0.1 mol%), as shown in Figure S10a. Additional solvent (DMF:DMSO (3:1, v/v)) was then added to adjust the final volume in each well to 50 µL while not compromising the final concentration of $Cs_{0.15}FA_{0.85}PbI_3$ HP to be 1.0 M. Microcrystal formation was induced by rapidly injecting chloroform 200 µL as an antisolvent, and the appearance of microcrystals was visually confirmed.

The synthesized HP microplate was immediately loaded into a multi-mode optical reader (Synergy H1, Agilent). Time-evolved photoluminescence (PL) spectra were collected from the bottom of the plate. Emission spectra (450–800 nm, 1 nm step) were collected under 365 nm excitation by scanning the wells sequentially. Spectra from all 96 wells were recorded every 15 min as consecutive "read cycles." The read cycles were repeated at 50°C for 6 h. The PL signals were collected at 7 mm below the microplate bottom via sweep mode. A narrow-sized excitation spot (<3 mm in diameter) was used by adjusting the aperture, thereby suppressing the emission crosstalk.

4.4 | Characterizations

UV–vis absorption spectra were measured with a UV-2600 spectrometer (Shimadzu). ^{1}H-NMR spectra were collected using a 400 MHz FT-NMR spectrometer (Bruker, Avance III 400). DLS measurements were performed using the ELS-Z1000 (Otsuka Electronics) at the Center for Research Equipment, Yonsei University (Seoul). In situ PL measurements were performed during the spin-coating and thermal annealing processes using a 405 nm continuous wave laser as the excitation source, with the emitted PL collected by a fiber (M147L01; 400 µm, 0.22NA) coupled SR4 spectrometer (Ocean Optics) through a 450 nm long-pass filter to suppress the excitation laser. GIWAXS measurements were conducted at the 3C SAXS-I and 9A beamline of Pohang Accelerator Laboratory in Pohang, Republic of Korea. AFM and KPFM were conducted using an NX10 AFM (Park Systems) at the Center for Polymers and Composite Materials. SEM imaging of HP films was performed using a Sigma 300 VP scanning electron microscope (Carl Zeiss) at the Center for Polymers and Composite Materials. The *J*–*V* curves of the solar cells were measured using an LCS-100 Series Small Area Solar Simulator under AM 1.5G 1 sun illumination (100 mW/cm^2), which was installed in an N_2-filled glove box with a Keithley 2400 Source Meter. A black shadow mask with an aperture area of 0.0314 cm^2 was used to prevent the overestimation of the photocurrent. EQE spectra were collected with a PV measurement QE system with monochromatic light from a xenon lamp. PL intensity maps

16163028, 2026, 49, Downloaded from https://advanced.onlinelibrary.wiley.com/doi/10.1002/adfm.75810 by Hanyang University Library, Wiley Online Library on [22/11/2026]. See the Terms and Conditions (https://onlinelibrary.wiley.com/terms-and-conditions) on Wiley Online Library for rules of use; OA articles are governed by the applicable Creative Commons License

were captured by using an upright-type PL microscope (Nikon, Eclipse LV-100ND) with a 100× objective lens and a 385 nm LED light source as an excitation source. The resulting PL emission maps, after passing a long-pass filter to exclude the stray UV light, were subsequently collected by using a 2k CMOS-type microscope camera (Nikon DS-10), with an acquisition time of 1 min. ToF-SIMS measurements were conducted using a TOF-SIMS 5 instrument (IONTOF GmbH) at the Ulsan National Institute of Science and Technology (UNIST), Ulsan, Republic of Korea, to investigate the depth-dependent distribution of chemical species in the perovskite films. The samples were analyzed using a pulsed Bi^+ primary ion beam (25 keV, 1.00 pA). As Bi^+ primary ion beam was used for analysis rather than sputtering, depth profiling was performed by alternating analysis and sputtering cycles. Sputtering was carried out using a Cs^+ ion beam (0.5 keV, 35 nA) for negative ion mode. The analysis (scan) area was set to 50 × 50 μm^2, while the sputtering area was 250 × 250 μm^2.

4.5 | Fabrication of PSCs

For precursor preparation, $FAPbI_3$ was synthesized by dissolving stoichiometric FAI and PbI_2 in 2-methoxyethanol (2-ME; 0.6 M), stirring until complete dissolution, filtering through a 0.45 μm PVDF membrane filter, and heating in a round-bottom flask to ~120°C. As the reaction progressed, a black precipitate gradually appeared, after which chlorobenzene was slowly added dropwise to promote crystallization. The precipitate was collected by filtration and washed with diethyl ether. $MAPbBr_3$ was synthesized by dissolving MABr and $PbBr_2$ in DMF (1.2 M), followed by recrystallization in an oil bath at 100°C for several hours until crystal precipitation occurred. The product was filtered, washed with diethyl ether, and dried for further use.

p-i-n-type PSCs were fabricated with the structure FTO/SAM/$Cs_{0.05}MA_{0.05}FA_{0.90}Pb(I_{0.95}Br_{0.05})_3$/$C_{60}$/BCP/Ag. FTO patterned glass substrates (1.5 × 1.5 cm^2, sheet resistance: 7 Ω/cm^2) were sequentially cleaned by sonication in detergent, acetone, and 2-propanol, and then followed by ultraviolet-ozone treatment for 20 min. These substrates were then transferred into the N_2-filled glove box. Self-assembled monolayer (SAM) molecules of 4PADCB (0.5 mg/mL in ethanol) were spin-coated on the FTO substrate at 3000 rpm for 30 s and subsequently annealed at 100°C for 10 min. The HP precursor solution was prepared by dissolving $FAPbI_3$ (90%), $MAPbBr_3$ (5%), and CsI (5%), with excess PbI_2 (10%), MACl (15%), and EDTA-salt ($EDTA^{2-}$, $EDTA^{4-}$, 0.3%) as additives in DMF:DMSO (4:1, v/v) solvent system at a total concentration of 1.8 M. The HP films were deposited by spin-coating the solution onto the SAM molecule-coated substrates at 4000 rpm for 40 s. During spinning, 0.5 mL of ethyl acetate (EA) was rapidly dropped in the final 10 s, followed by thermal annealing at 100°C for 60 min. A solution of $PDAI_2$ (0.5 mg/mL in IPA) was spin-coated onto the HP layer at 3000 rpm for 30 s, followed by thermal annealing at 100°C for 5 min. Electron transport layers and electrodes were deposited by thermal evaporation under ~10^{-6} Torr. A 23 nm C_{60} layer was deposited at a rate of 0.2–0.4 Å/s, followed by 5 nm BCP at 0.1–0.2 Å/s and 100 nm Ag at 0.1–1 Å/s.

Acknowledgements

This work was supported by the National Research Foundation of Korea (NRF) grant funded by the Korea government (MSIT). (RS-2024-00436187, RS-2023-00266946, RS-2025-00560645). This research was also supported by the Global-Learning and Academic Research Institution for Master's. Ph.D students and Postdocs (LAMP) Program of the National Research Foundation of Korea (NRF) grant funded by the Ministry of Education (No. RS-2024-00442483). This research was supported by the Korea Basic Science Institute (National Research Facilities and Equipment Center) grant funded by the Ministry of Education (2022R1A6C101A779).

Conflicts of Interest

The authors declare no conflicts of interest.

Data Availability Statement

The data that support the findings of this study are available from the corresponding author upon reasonable request.

References

1. B. Dong, M. Wei, Y. Li, et al., "Self-Assembled Bilayer for Perovskite Solar Cells with Improved Tolerance against Thermal Stresses," *Nature Energy* 10 (2025): 342, https://doi.org/10.1038/s41560-024-01689-2.

2. M. A. Green, E. D. Dunlop, M. Yoshita, et al., "Solar Cell Efficiency Tables (Version 66)," *Progress in Photovoltaics: Research and Applications* 33: 795–810, https://doi.org/10.1002/pip.3919.

3. G. Li, Z. Zhang, B. Agyei-Tuffour, et al., "Stabilizing High-Efficiency Perovskite Solar Cells via Strategic Interfacial Contact Engineering," *Nature Photonics* 20 (2026): 55–62, https://doi.org/10.1038/s41566-025-01791-1.

4. H. Song, H.-B. Kim, S. C. Cho, et al., "Supramolecular Design Principles in Pseudohalides for High-Performance Perovskite Solar Mini Modules," *Joule* 8 (2024): 2283–2303, https://doi.org/10.1016/j.joule.2024.05.019.

5. H. Song, J. Won, H.-B. Kim, et al., "Refining Multiscale Heterogeneity in Perovskite Solar Cells via Interfacial Chemistry Homogenization," *Advanced Functional Materials* 35 (2025): 2421402, https://doi.org/10.1002/adfm.202421402.

6. T. D. Raju, V. Murugadoss, K. A. Nirmal, T. D. Dongale, A. V. Kesavan, and T. G. Kim, "Advancements in Perovskites for Solar Cell Commercialization: a Review," *Advanced Powder Materials* 4 (2025): 100275, https://doi.org/10.1016/j.apmate.2025.100275.

7. M.-I. Jamesh, H. Tong, M. Du, et al., "Advancement of Technology Towards Developing Perovskite-Based Solar Cells for Renewable Energy Harvesting and Energy Transformation Applications," *npj Materials Sustainability* 3 (2025): 29, https://doi.org/10.1038/s44296-025-00073-9.

8. M. Lee, L. Wang, D. Zhang, et al., "Scanning Probe Microscopy of Halide Perovskite Solar Cells," *Advanced Materials* 36 (2024): 2407291, https://doi.org/10.1002/adma.202407291.

9. Z. Ren, B. Tuo, N. Wang, et al., "Advances in Intermediates for the Solution-Processing of Perovskite Films," *CCS Chemistry* 6 (2024): 585–603, https://doi.org/10.31635/ccschem.023.202302989.

10. Z. Wu, S. Sang, J. Zheng, et al., "Crystallization Kinetics of Hybrid Perovskite Solar Cells," *Angewandte Chemie International Edition* 63 (2024): 202319170, https://doi.org/10.1002/anie.202319170.

11. F. Jiang, Y. Shi, T. R. Rana, et al., "Improved Reverse Bias Stability in p–i–n Perovskite Solar Cells with Optimized Hole Transport Materials and Less Reactive Electrodes," *Nature Energy* 9 (2024): 1275–1284, https://doi.org/10.1038/s41560-024-01600-z.

12. D. Liu, Y. Wu, M. R. Samatov, A. S. Vasenko, E. V. Chulkov, and O. V. Prezhdo, "Compression Eliminates Charge Traps by Stabilizing Perovskite Grain Boundary Structures: an Ab Initio Analysis with Machine

16163028, 2026, 49, Downloaded from https://advanced.onlinelibrary.wiley.com/doi/10.1002/adfm.75810 by Hanyang University Library, Wiley Online Library on [22/11/2026]. See the Terms and Conditions (https://onlinelibrary.wiley.com/terms-and-conditions) on Wiley Online Library for rules of use; OA articles are governed by the applicable Creative Commons License

Learning Force Field," *Chemistry of Materials* 36 (2024): 2898–2906, https://doi.org/10.1021/acs.chemmater.3c03261.

13. K. Yan, M. Long, T. Zhang, et al., "Hybrid Halide Perovskite Solar Cell Precursors: Colloidal Chemistry and Coordination Engineering behind Device Processing for High Efficiency," *Journal of the American Chemical Society* 137 (2015): 4460–4468, https://doi.org/10.1021/jacs.5b00321.

14. A.-F. Castro-Méndez, J. Hidalgo, and J.-P. Correa-Baena, "The Role of Grain Boundaries in Perovskite Solar Cells," *Advanced Energy Materials* 9 (2019): 1901489, https://doi.org/10.1002/aenm.201901489.

15. D. Zhang, D. Li, Y. Hu, A. Mei, and H. Han, "Degradation Pathways in Perovskite Solar Cells and How to Meet International Standards," *Communications Materials* 3 (2022): 58, https://doi.org/10.1038/s43246-022-00281-z.

16. R. Li, Z. Sun, L. Yao, et al., "Unraveling the Degradation Mechanisms of Perovskite Solar Cells under Mechanical Tensile Loads," *ACS Nano* 18 (2024): 24495–24504, https://doi.org/10.1021/acsnano.4c08378.

17. H. Zhu, S. Teale, M. N. Lintangpradipto, et al., "Long-Term Operating Stability in Perovskite Photovoltaics," *Nature Reviews Materials* 8 (2023): 569–586, https://doi.org/10.1038/s41578-023-00582-w.

18. B. Li, D. Binks, G. Cao, and J. Tian, "Engineering Halide Perovskite Crystals through Precursor Chemistry," *Small* 15 (2019): 1903613, https://doi.org/10.1002/smll.201903613.

19. E. Radicchi, E. Mosconi, F. Elisei, F. Nunzi, and F. De Angelis, "Understanding the Solution Chemistry of Lead Halide Perovskites Precursors," *ACS Applied Energy Materials* 2 (2019): 3400–3409, https://doi.org/10.1021/acsaem.9b00206.

20. N. J. Jeon, J. H. Noh, Y. C. Kim, W. S. Yang, S. Ryu, and S. I. Seok, "Solvent Engineering for High-Performance Inorganic–organic Hybrid Perovskite Solar Cells," *Nature Materials* 13 (2014): 897–903, https://doi.org/10.1038/nmat4014.

21. N. N. Intan, B. A. Sorenson, Y. K. Choi, et al., "Smaller Is Better: the Case for Lower-Order Iodoplumbate Species Dominating $MAPbI_3$ /Dimethylformamide Solutions," *Chemistry of Materials* 36 (2024): 8424–8436, https://doi.org/10.1021/acs.chemmater.4c01523.

22. M. A. Flatken, A. Hoell, R. Wendt, et al., "Small-Angle Scattering to Reveal the Colloidal Nature of Halide Perovskite Precursor Solutions," *Journal of Materials Chemistry A* 9 (2021): 13477–13482, https://doi.org/10.1039/D1TA01468D.

23. S.-H. Cho, S. C. Cho, S.-J. Chang, S. U. Lee, and N.-G. Park, "Solution-Phase PbI_2 Coordination Controls Perovskite Film Formation and Photovoltaic Performance," *ACS Energy Letters* 10 (2025): 3931–3940, https://doi.org/10.1021/acsenergylett.5c01854.

24. W. Chen, S. Zhou, H. Cui, et al., "Universal in Situ Oxide-Based ABX_3-Structured Seeds for Templating Halide Perovskite Growth in All-Perovskite Tandems," *Nature Communications* 16 (2025): 1894, https://doi.org/10.1038/s41467-025-57195-w.

25. P. Ahlawat, C. Clementi, F. Musil, M.-A. Filip, and M. I. Dar, "Lattice-Matched Heterogeneous Nucleation Eliminates Defective Buried Interfaces in Halide Perovskites," *Chemistry of Materials* 37 (2025): 2177–2191, https://doi.org/10.1021/acs.chemmater.4c03034.

26. P. Shi, Y. Ding, B. Ding, et al., "Oriented Nucleation in Formamidinium Perovskite for Photovoltaics," *Nature* 620 (2023): 323–327, https://doi.org/10.1038/s41586-023-06208-z.

27. S. Srivastava, S. Ranjan, H. Suman, et al., "Tailoring Precursor-Solvent Coordination Controls the Crystallization Kinetics and Nuclei Growth for Phase Homogenization in Wide-Bandgap Perovskite Solar Cells," *Advanced Science* 12 (2025): 07660.

28. J.-W. Lee, H.-S. Kim, and N.-G. Park, "Lewis Acid–Base Adduct Approach for High Efficiency Perovskite Solar Cells," *Accounts of Chemical Research* 49 (2016): 311–319, https://doi.org/10.1021/acs.accounts.5b00440.

29. B. Yang, J. Suo, D. Bogachuk, et al., "A Universal Ligand for Lead Coordination and Tailored Crystal Growth in Perovskite Solar Cells," *Energy & Environmental Science* 17 (2024): 1549–1558, https://doi.org/10.1039/D3EE02344C.

30. S. Luo, S. Cao, T. Zheng, et al., "Melamin Holding PbI_2 with Three "Arms": an Effective Chelation Strategy to Control the Lead Iodide to Perovskite Conversion for Inverted Perovskite Solar Cells," *Energy & Environmental Science* 18 (2025): 2436–2451, https://doi.org/10.1039/D4EE04692G.

31. M. Liu, J. Zhang, S. Qin, et al., "Efficient and Stable p–i–n Perovskite Solar Cells Enabled by in Situ Functional Group Conversion," *Journal of the American Chemical Society* 146 (2024): 32105–32116, https://doi.org/10.1021/jacs.4c13248.

32. Y.-K. Wang, D. Ma, F. Yuan, et al., "Chelating-Agent-Assisted Control of $CsPbBr_3$ Quantum Well Growth Enables Stable Blue Perovskite Emitters," *Nature Communications* 11 (2020): 3674, https://doi.org/10.1038/s41467-020-17482-0.

33. H. Butovych, F. Keshavarz, B. Barbiellini, E. Lähderanta, J. Ilnytskyi, and T. Patsahan, "Role of EDTA Protonation in Chelation-Based Removal of Mercury Ions from Water," *Physical Chemistry Chemical Physics* 26 (2024): 25402–25411, https://doi.org/10.1039/D4CP02980A.

34. J. E. Tackett and D. T. Sawyer, "Structure of Sodium Ethylenediaminetetraacetic Acid in Aqueous Solution," *Inorganic Chemistry* 3 (1964): 304, https://doi.org/10.1021/ic50012a053.

35. A. Kovács, D. S. Nemcsok, and T. Kocsis, "Bonding Interactions in EDTA Complexes," *Journal of Molecular Structure: THEOCHEM* 950 (2010): 93–97, https://doi.org/10.1016/j.theochem.2010.03.036.

36. B. Nowack, "Environmental Chemistry of Aminopolycarboxylate Chelating Agents," *Environmental Science & Technology* 36 (2002): 4009–4016, https://doi.org/10.1021/es025683s.

37. J. C. Hamill Jr., J. Schwartz, and Y.-L. Loo, "Influence of Solvent Coordination on Hybrid Organic–Inorganic Perovskite Formation," *ACS Energy Letters* 3 (2018): 92–97, https://doi.org/10.1021/acsenergylett.7b01057.

38. R. A. Kerner, K. P. White, N. Balasubramaniam, et al., "Why Are Lead Iodide-Based Perovskite Precursor Inks Yellow?," *Advanced Energy Materials* 16 (2026): 02813.

39. Y. Hassan, J. H. Park, M. L. Crawford, et al., "Ligand-Engineered Bandgap Stability in Mixed-Halide Perovskite LEDs," *Nature* 591 (2021): 72–77, https://doi.org/10.1038/s41586-021-03217-8.

40. Y. Lu, H. Zhu, S. Tan, et al., "Stabilization of Organic Cations in Lead Halide Perovskite Solar Cells Using Phosphine Oxides Derivatives," *Journal of the American Chemical Society* 146 (2024): 22387–22395, https://doi.org/10.1021/jacs.4c05398.

41. M. Li, R. Sun, J. Chang, et al., "Orientated Crystallization of FA-Based Perovskite via Hydrogen-Bonded Polymer Network for Efficient and Stable Solar Cells," *Nature Communications* 14 (2023): 573, https://doi.org/10.1038/s41467-023-36224-6.

42. J. Hu, Z. Xu, T. L. Murrey, et al., "Triiodide Attacks the Organic Cation in Hybrid Lead Halide Perovskites: Mechanism and Suppression," *Advanced Materials* 35 (2023): 2303373, https://doi.org/10.1002/adma.202303373.

43. M. Novakovic, Ē. Kupče, A. Oxenfarth, et al., "Sensitivity Enhancement of Homonuclear Multidimensional NMR Correlations for Labile Sites in Proteins, Polysaccharides, and Nucleic Acids," *Nature Communications* 11 (2020): 5317, https://doi.org/10.1038/s41467-020-19108-x.

44. M. Novakovic, M. D. Battistel, H. F. Azurmendi, M.-G. Concilio, D. I. Freedberg, and L. Frydman, "The Incorporation of Labile Protons into Multidimensional NMR Analyses: Glycan Structures Revisited," *Journal of the American Chemical Society* 143 (2021): 8935–8948, https://doi.org/10.1021/jacs.1c04512.

45. J. Yang, B. J. Lawrie, S. V. Kalinin, and M. Ahmadi, "High-Throughput Automated Exploration of Phase Growth Behaviors in Quasi-2D

16163028, 2026, 49, Downloaded from https://advanced.onlinelibrary.wiley.com/doi/10.1002/adfm.75810 by Hanyang University Library, Wiley Online Library on [22/11/2026]. See the Terms and Conditions (https://onlinelibrary.wiley.com/terms-and-conditions) on Wiley Online Library for rules of use; OA articles are governed by the applicable Creative Commons License

Formamidinium Metal Halide Perovskites," *Advanced Energy Materials* 13 (2023): 2302337, https://doi.org/10.1002/aenm.202302337.

46. J. Yang, D. K. LaFollette, B. J. Lawrie, et al., "Understanding the Role of Cesium on Chemical Complexity in Methylammonium-Free Metal Halide Perovskites," *Advanced Energy Materials* 13 (2023): 2202880, https://doi.org/10.1002/aenm.202202880.

47. M. Hao, J. Yang, W. Yu, et al., "Nanoscopic Cross-Grain Cation Homogenization in Perovskite Solar Cells," *Nature Nanotechnology* 20 (2025): 630–638, https://doi.org/10.1038/s41565-025-01854-y.

48. M. Othman, Q. Jeangros, D. A. Jacobs, et al., "Alleviating Nanostructural Phase Impurities Enhances the Optoelectronic Properties, Device Performance and Stability of Cesium-Formamidinium Metal–Halide Perovskites," *Energy & Environmental Science* 17 (2024): 3832–3847, https://doi.org/10.1039/D4EE00901K.

49. S. Shin, Y. Yu, H. Song, et al., "High-Throughput Automated Discovery of Temperature Benign Dion-Jacobson Quasi-2D Halide Perovskites," *ChemRxiv* (2025): chemrxiv-2025-m0l72, https://doi.org/10.26434/chemrxiv-2025-m0l72.

50. M. Um, S. L. Sanchez, H. Song, et al., "Tailoring Molecular Space to Navigate Phase Complexity in Cs-Based Quasi-2D Perovskites via Gated-Gaussian-Driven High-Throughput Discovery," *Advanced Energy Materials* 15 (2025): 2404655, https://doi.org/10.1002/aenm.202404655.

51. J. Yang, J. Hidalgo, D. Song, S. V. Kalinin, J.-P. Correa-Baena, and M. Ahmadi, "Accelerating Materials Discovery by High-Throughput GIWAXS Characterization of Quasi-2D Formamidinium Metal Halide Perovskites," *Advanced Functional Materials* 34 (2024): 2409293, https://doi.org/10.1002/adfm.202409293.

52. T. Huang, S. Tan, S. Nuryyeva, et al., "Performance-Limiting Formation Dynamics in Mixed-Halide Perovskites," *Science Advances* 7 (2021): abj1799, https://doi.org/10.1126/sciadv.abj1799.

53. Y. An, N. Zhang, Z. Zeng, et al., "Optimizing Crystallization in Wide-Bandgap Mixed Halide Perovskites for High-Efficiency Solar Cells," *Advanced Materials* 36 (2024): 2306568, https://doi.org/10.1002/adma.202306568.

54. F. Li, X. Deng, Z. Shi, et al., "Hydrogen-Bond-Bridged Intermediate for Perovskite Solar Cells with Enhanced Efficiency and Stability," *Nature Photonics* 17 (2023): 478–484, https://doi.org/10.1038/s41566-023-01180-6.

55. M. Qin, K. Tse, T.-K. Lau, et al., "Manipulating the Mixed-Perovskite Crystallization Pathway Unveiled by in Situ GIWAXS," *Advanced Materials* 31 (2019): 1901284, https://doi.org/10.1002/adma.201901284.

56. G. Bravetti, N. Taurisano, A. Moliterni, et al., "Solution Aging Promotes the Formation of Hexagonal Polytypes in Mixed-Cation/-Halide Perovskites," *Chemistry of Materials* 36 (2024): 3150–3163, https://doi.org/10.1021/acs.chemmater.3c02694.

57. D. Liu, D. Luo, A. N. Iqbal, et al., "Strain Analysis and Engineering in Halide Perovskite Photovoltaics," *Nature Materials* 20 (2021): 1337–1346, https://doi.org/10.1038/s41563-021-01097-x.

58. D.-K. Lee, K. Fykouras, T. Kodalle, et al., "Strain Engineering: Reduction of Microstrain at the Perovskite Surface via Alkali Metal Chloride Treatment Enhances Stability," *ACS Energy Letters* 10 (2025): 1039–1049, https://doi.org/10.1021/acsenergylett.4c03334.

59. H. Yoon, S. Hong, S. H. Lee, I. H. Cho, and H. J. Kim, "GIWAXS Analysis on Preferred Orientation in Metal Halide Perovskite Films via Alkylamines," *Electronic Materials Letters* 18 (2022): 456–464, https://doi.org/10.1007/s13391-022-00352-w.

60. Y. Yao, B. Li, D. Ding, et al., "Oriented Wide-Bandgap Perovskites for Monolithic Silicon-Based Tandems with over 1000 Hours Operational Stability," *Nature Communications* 16 (2025): 40, https://doi.org/10.1038/s41467-024-55377-6.

61. M. Li, Y. Jiang, S. Chen, et al., "Radical Molecular Network-Buffer Minimizes Photovoltage Loss in $FAPbI_3$ Perovskite Solar Cells," *Advanced Materials* 37 (2025): 2417289, https://doi.org/10.1002/adma.202417289.

62. T. Yang, Y. Yang, T. Niu, et al., "Facet Orientation-Dependent Strain Relaxation Stabilizes $FAPbI_3$ Perovskite Solar Cells," *ACS Energy Letters* 10 (2025): 427–438, https://doi.org/10.1021/acsenergylett.4c02674.

63. S. Zhang, Y. Zhou, Z. Shen, et al., "High-Efficiency and Stable Perovskite Solar Cells via Bidentate Chelation for Facet-Engineered Growth of $FAPbI_3$ (111) Crystals," *Chemical Engineering Journal* 516 (2025): 164079, https://doi.org/10.1016/j.cej.2025.164079.

64. J. Nie, Y. Zhang, J. Wang, L. Li, and Y. Zhang, "Recent Progress in Regulating Surface Potential for High-Efficiency Perovskite Solar Cells," *ACS Energy Letters* 9 (2024): 1674–1681, https://doi.org/10.1021/acsenergylett.4c00240.

65. X. Yuan, H. Lei, and C. Chen, "An Ethylenediaminetetraacetic Acid (EDTA) Surface-Functionalized CeO_2 Composite Abrasives with the Effective Improvement of the Removal Rate on Glass CMP," *Ceramics International* 50 (2024): 293–305, https://doi.org/10.1016/j.ceramint.2023.10.103.

66. Y. W. Woo, Z. Li, Y.-K. Jung, J.-S. Park, and A. Walsh, "Inhomogeneous Defect Distribution in Mixed-Polytype Metal Halide Perovskites," *ACS Energy Letters* 8 (2023): 356–360, https://doi.org/10.1021/acsenergylett.2c02306.

67. H. Kim, S.-M. Yoo, B. Ding, et al., "Shallow-Level Defect Passivation by 6H Perovskite Polytype for Highly Efficient and Stable Perovskite Solar Cells," *Nature Communications* 15 (2024): 5632, https://doi.org/10.1038/s41467-024-50016-6.

68. T. A. S. Doherty, S. Nagane, D. J. Kubicki, et al., "Stabilized Tilted-Octahedra Halide Perovskites Inhibit Local Formation of Performance-Limiting Phases," *Science* 374 (2021): 1598–1605, https://doi.org/10.1126/science.abl4890.

Supporting Information

Additional supporting information can be found online in the Supporting Information section.

Supporting File: adfm75810-sup-0001-SuppMat.docx.

16163028, 2026, 49, Downloaded from https://advanced.onlinelibrary.wiley.com/doi/10.1002/adfm.75810 by Hanyang University Library, Wiley Online Library on [22/11/2026]. See the Terms and Conditions (https://onlinelibrary.wiley.com/terms-and-conditions) on Wiley Online Library for rules of use; OA articles are governed by the applicable Creative Commons License